www.acsnano.org

Hyperbolic Polaritonic Rulers Based on van der Waals α -MoO₃ Waveguides and Resonators

Shang-Jie Yu, Helen Yao, Guangwei Hu, Yue Jiang, Xiaolin Zheng, Shanhui Fan, Tony F. Heinz, and Jonathan A. Fan*



Downloaded via STANFORD UNIV on January 24, 2024 at 21:59:55 (UTC). See https://pubs.acs.org/sharingguidelines for options on how to legitimately share published articles.

Cite This: ACS Nano 2023, 17, 23057-23064



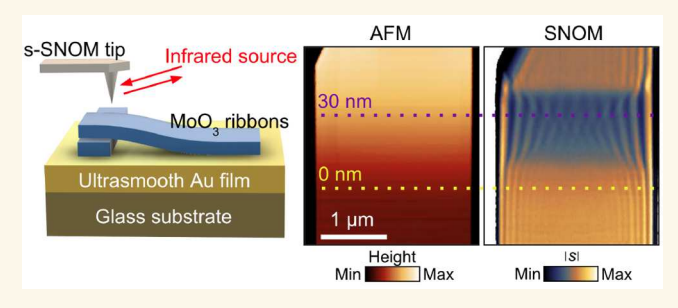
ACCESS I

III Metrics & More

Article Recommendations

s Supporting Information

ABSTRACT: Low-dimensional, strongly anisotropic nanomaterials can support hyperbolic phonon polaritons, which feature strong light—matter interactions that can enhance their capabilities in sensing and metrology tasks. In this work, we report hyperbolic polaritonic rulers, based on microscale α -phase molybdenum trioxide (α -MoO₃) waveguides and resonators suspended over an ultraflat gold substrate, which exhibit near-field polaritonic characteristics that are exceptionally sensitive to device geometry. Using scanning near-field optical microscopy, we show that these systems support strongly confined image polariton modes that exhibit ideal



antisymmetric gap polariton dispersion, which is highly sensitive to air gap dimensions and can be described and predicted using a simple analytic model. Dielectric constants used for modeling are accurately extracted using near-field optical measurements of α -MoO₃ waveguides in contact with the gold substrate. We also find that for nanoscale resonators supporting in-plane Fabry-Perot modes, the mode order strongly depends on the air gap dimension in a manner that enables a simple readout of the gap dimension with nanometer precision.

KEYWORDS: nanophotonics, polaritonics, van der Waals materials, near-field optical microscopy, nanometrology

anophotonic systems with highly sensitive geometrydependent optical responses are fundamental to a broad range of scientific phenomena and technological concepts. Systems supporting near-field-coupled nanostructures are the basis of many sensors due to their support of strongly confined optical modes that are sensitive to the variation of geometry and refractive index. Optical MEMS utilize small changes in structural configuration to produce large changes in phase shift or coloration, which have applications in displays and metrology instrumentation.^{1,2} In optomechanics, coupling between photons and mechanical motions can lead to strongly nonlinear optical transduction phenomena.^{3,4} While significant progress has been made to elucidate these system configurations at visible wavelengths, the development of such systems in the mid-infrared range has proven to be challenging for at least two reasons. First, wavelengths in the mid-infrared range are relatively long, and the direct scaling of sensor or MEMS concepts from visible to infrared wavelengths typically leads to microscale systems with reduced geometry-dependent sensitivity. Second, the properties of conventional materials at infrared wavelengths diverge from those at visible frequencies. For example, typical metals

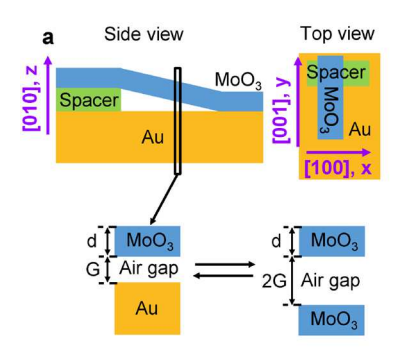
are no longer plasmonic but behave more as ideal conductors, and many dielectric materials strongly absorb.

Recent advances in materials science and metrology have presented opportunities to configure and characterize nanophotonic infrared systems. In particular, a class of phononpolaritonic (PhP) materials, including α -phase molybdenum trioxide $(\alpha\text{-MoO}_3)$, ^{5–7} hexagonal boron nitride, ^{8–10} and α -phase vanadium oxide, ¹¹ have been shown by scattering-type scanning near-field optical microscopy (SNOM) to enable strong wave confinement and high field enhancement properties at infrared wavelengths. ^{12–15} These enhanced light–matter interactions yield extraordinary sensitivity to local environmental changes, ^{16,17} and various studies have indicated the potential for small variations in geometry and dielectric

Received: September 12, 2023 Revised: November 5, 2023 Accepted: November 7, 2023 Published: November 10, 2023







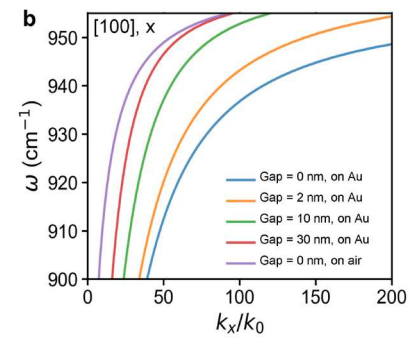


Figure 1. Image polaritons in an α -MoO₃ microribbon-air gap-gold structure. (a) Schematic of the tapered structure with a d-thick flake and an optically thick gold substrate. The air gap G continuously varies along the taper, and lateral sections of the structure can be optically modeled as two identical microribbons separated by 2G. (b) Theoretical antisymmetric gap mode dispersion relations of the polaritonic ruler with different gap sizes and substrates, which indicate the strong sensitivity of PhP wavevector to local geometry.

environment to be manifested as large optical signals. For example, researchers have investigated the sensitivity of PhP dispersion to the substrate material, ^{18–26} including ideal metal substrates, ^{27,28} and have examined the potential of microstructured PhP devices as sensors. ²⁹

We present α -MoO₃ microribbons suspended over an ultrasmooth gold film as a model system for studying the transduction of nanoscale geometric variations to optical nearfield signals within polaritonic devices. This polaritonic ruler system serves as an analogue to visible light plasmonic rulers,^{30–32} as it uses strong light confinement and dispersion sensitivity of PhP materials to enable nanoscale geometric sensing. Our focus is on microribbons that form self-assembled tapered structures over the gold film (Figure 1a), which enable the study of PhP modes with continuously varying air gap dimensions as a function of spatial position. Experimentally, we characterize structures made from high-quality α -MoO₃ microribbons synthesized by flame vapor deposition (FVD), which feature atomically smooth sidewalls and optical properties consistent with ideal exfoliated α -MoO₃ material.³³ Using the same high-quality microribbons reported in ref 33, we experimentally study the gap modes with infrared SNOM. Our results match well with a simple analytic model, which we use to analyze the strong PhP dispersion sensitivity of these systems and identify device configurations that maximize device sensitivity to gap variations. We also achieve accurate predictions of the gap size by imaging and fitting the PhP wavelength and the Fabry-Pérot (FP) mode order within the tapered structures with the analytic model. We note a recent study involving the analysis of an α -MoO₃ tapered waveguide structure placed over a low-contrast dielectric substrate, which also examines PhP sensitivity with gap size but requires more complex modeling and possesses limited sensitivity metrics.²¹

RESULTS

In our tapered microribbon–gold substrate system (α -MoO₃ ribbon thickness d), we consider gaps that adiabatically vary from 0 to 35 nm, such that local submicrometer regions within the system can be approximated as an α -MoO₃ structure with a constant gap G (Figure 1a). The gold substrate is atomically smooth and produced using template stripping methods, ^{34,35} which produces ideal metal material interfaces with negligible roughness. At mid-infrared wavelengths, the gold behaves close to a perfect electrical conductor (PEC), ³⁶ and in the limit where we approximate the substrate as a PEC, the α -MoO₃

microribbon produces an ideal image polariton in the conducting substrate (Figure 1a, lower left). The electric field at the dielectric gap/gold interface is then zero due to the boundary conditions and can only support antisymmetric modes. The optical modes in the α -MoO $_3$ microribbon—air gap—gold system in this limit can be described as the fundamental antisymmetric gap mode (i.e., l=0) supported by two α -MoO $_3$ ribbons separated by a gap with distance 2G (Figure 1a, lower right). The analytic dispersion relations of such modes can be readily derived from the source-free Maxwell equations (see theSupporting Information) and is given by

$$k_{x(y)} = \frac{\psi}{d} \left[\arctan \left(\varepsilon_1 \frac{\psi}{\varepsilon_z} \right) + \arctan \left(\frac{\varepsilon_G}{\tanh(k_{x(y)}G)} \frac{\psi}{\varepsilon_z} \right) + l\pi \right]$$
(1)

where $k_{x(y)}$ is the wavevector propagating along the crystal x-axis (y-axis), $\varepsilon_{x/y/z}$ is the α -MoO₃ permittivity, which is anisotropic, ε_G is the permittivity of the gap material, ε_1 is the top material's permittivity, the parameter $\psi = \sqrt{-\frac{\varepsilon_z}{\varepsilon_{x(y)}}}$, and $l = \frac{\varepsilon_z}{\varepsilon_{x(y)}}$

0, 1, 2, ... parametrizes the different mode orders. We assume the crystal *x*-axis is oriented along the [100] direction, and the crystal *y*-axis is oriented along the [001] direction, as shown in Figure 1a. For this study, we will focus on frequencies in the 900–1000 cm⁻¹ range, which overlaps with the α -MoO₃ Reststrahlen band (see the Supporting Information) and yields hyperbolic PhP modes with $\varepsilon_x < 0$ and $\varepsilon_{yz} > 0$.

Equation 1 has an explicit dependence on gap size and gap permittivity, and as such, these parameters serve as a transduction mechanism that can strongly influence the mode dispersion of the system. We note that this dispersion equation is a generalized form of several previous findings. For example, when G is limited to infinity, the tanh(*) term becomes 1. This limit corresponds to the situation where α - MoO_3 is placed on a single substrate with ε_G , agreeing with previous derivations. When G becomes 0, $\varepsilon_G/\tanh(k_{x(y)}G)$ diverges and the second term becomes $-\pi$ when $\varepsilon_z > 0$ or π when ε_z < 0. This limit corresponds to the image polariton picture. Our work falls between these two limits in which polariton dispersion strongly depends on the gap size and materials, naturally leading to the manifestation of the polariton ruler concept. As an example, we theoretically quantify the impact of different air gap sizes on fundamental mode dispersion by utilizing α -MoO₃ permittivity values from

previous studies 40,41 in our analytic expression. These mode dispersion plots are shown in Figure 1b (also see the Supporting Information), with dielectric data taken from ref 40, and they indicate that for fixed wavelength and increasing gap size, the mode wavevector strongly shifts. For frequencies below the Reststrahlen band, the wavevector shifts to smaller values as a function of the increasing gap size. When the gap is 30 nm, the dispersion curves nearly converge to those of a freely suspended $\alpha\text{-MoO}_3$ ribbon, indicating the dynamic range of the polaritonic ruler as a sensor.

In order to experimentally correlate the optical properties of tapered α -MoO₃ ribbons with our analytical model, we first require an accurate assessment of the dielectric function of our material at our SNOM carbon dioxide laser source frequency, which is 935 cm⁻¹. Compared to large-area exfoliated samples used in prior dielectric characterization studies, our α -MoO₃ microstructures are synthesized by FVD and may support different dielectric constant properties. Uncertainties in the fitting process can also arise in the polarized far-field FTIR measurements. 40 We propose to use SNOM data from an ensemble of α -MoO₃ ribbons directly supported on ultraflat gold to evaluate the dielectric functions of these materials (see the Supporting Information). In this manner, we circumvent the spatial resolution limits in FTIR and Mueller matrix ellipsometry, 42 which is the standard for determining the dielectric function tensor of large-area films and flakes but which cannot be used on our microscale samples.

An optical microscopy image and measured SNOM fringe trace of a typical sample are shown in Figures 2a,b (see the Supporting Information for SNOM fringe fitting). SNOM has a typical spatial resolution of 15 nm, which is smaller than the

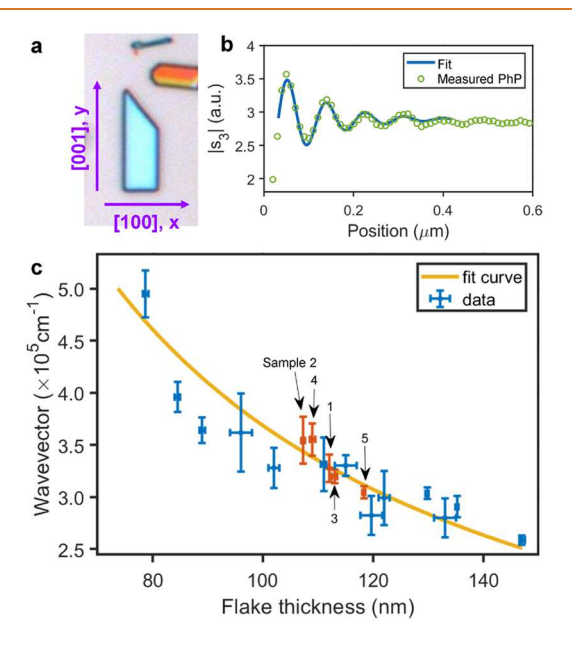


Figure 2. α -MoO₃ dielectric constant measurements based on SNOM image polariton characterization. (a) Optical microscopy image of an α -MoO₃ sample directly on top of an ultraflat gold substrate. (b) Representative fringe trace and fit from a SNOM scan of an α -MoO₃-gold substrate sample at 935 cm⁻¹. (c) Dielectric function fitting from 18 individual microribbon measurements. The samples highlighted in red have tapered sections used for gap-dependent PhP wavelength dispersion characterization in later sections.

minimal PhP wavelength of approximately 100 nm. A summary of experimental wavevectors for flakes of differing thicknesses is shown in Figure 2c for 18 different samples. The error bars in the plot are due to two sources: the limited instrument resolution and the variable quality of the samples measured. The role of limited SNOM image resolution is particularly enhanced for thinner microribbons, in which the mode wavevector increases as the ribbon thickness decreases. Variable sample quality can be manifested in the form of nonideal microribbon-gold interfaces, crystallographic defects in the α -MoO₃ ribbons, and subtle variations in thickness within individual ribbons. We note that the magnitudes of the error bars are consistent with those in prior studies involving the fitting of SNOM-measured PhP wavelengths in related phonon-polaritonic material systems.⁴³ In spite of these sources of noise, we consider our method to be the most accurate way to perform dielectric fitting due to the form factor of our samples.

With the experimental wavevectors and flake thicknesses, we use eq 1 with G=0 as a fitting function to extract the microribbon dielectric constant, which we measure to be $\varepsilon_x=-1.82$ and $\varepsilon_z=13.17$ at 935 cm⁻¹. As the configuration of the bulk of the α -MoO₃ ribbons does not contain crystallographic orientations in which ε_y is accessed, we were unable to accurately extract ε_y . These dielectric values are different from those measured from exfoliated flakes, ⁴⁰ and the origins of these differences will be a focus of a future study. This method of extracting dielectric functions from SNOM readout can be extended to other polaritonic nanomaterials such as hBN⁶ and $V_2O_{5,}^{11}$ which may not be available in bulk form, for convenient dielectric function fitting and extraction. We also anticipate that hyperspectral SNOM mapping ^{33,44} can be used to evaluate broad-band dielectric functions.

With experimentally obtained dielectric constants, we theoretically and experimentally analyzed tapered α -MoO₃ ribbons and characterized the dispersive gap mode properties of these hyperbolic polaritonic rulers. These tapers are selfassembled from the α -MoO₃ growth and dry transfer process, and they form when one end of the ribbon contacts the gold substrate, while the other point of contact is the top surface of a second ribbon. In this manner, the air gap between the tapered α -MoO₃ ribbon and the gold surface continuously varies. As these structures self-assemble during the dry transfer process, they are easily prepared without aligned or targeted transfer, and they are easy to find and probe due to the large quantity of available tapered ribbons. A representative tapered α -MoO₃ sample is shown in the black box in Figure 3a. The color gradient in the optical microscopy image, in which the color of the taper gradually changes from red to pink, is attributed to visible light interference manifested from the gradual variation in gap height. Figure 3b shows SNOM and atomic force microscopy (AFM) images of the device measured simultaneously, showing a taper region that is 2.4 μ m wide (along the x-direction) and 1.7 μ m long (along the ydirection). We extract the PhP fringes and the sample heights at different line cuts to produce a correlated result of gap height with PhP mode dispersion.

The measured SNOM fringe patterns along the α -axis (Figure 3c) show a clear dependence on gap height: the α -MoO₃ ribbon supports a highly compressed PhP wave ($\lambda \approx 100$ nm) when the ribbon touches the gold surface (G=0), and the PhP wavelength gradually gets larger as the gap increases. A detailed examination of four other tapered samples

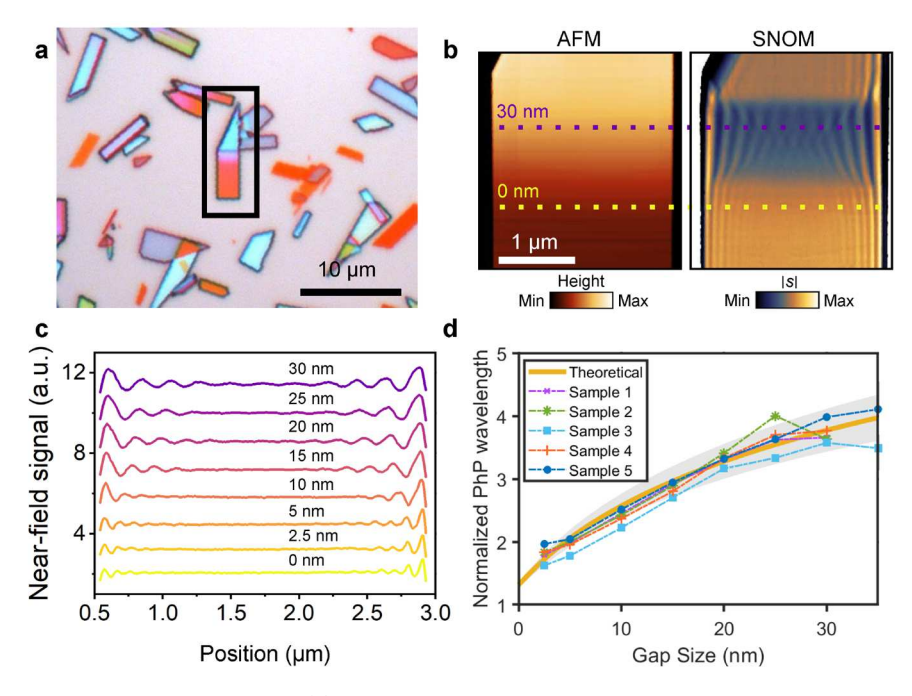


Figure 3. SNOM study of α -MoO₃ polaritonic rulers. (a) Optical microscopy image of a representative α -MoO₃ taper (black box, Sample 1 from Figure 2c). (b) Simultaneously measured AFM and SNOM images of the sample at 935 cm⁻¹. The dashed lines indicate two gap height positions determined by AFM. (c) Line cut profiles of the SNOM image at different gap sizes, which are denoted above each curve. The profiles are vertically offset for clarity. (d) Normalized theoretical and experimental PhP wavelength dependence on gap size using dielectric functions fit from Figure 2c and experimental PhP data from five tapered samples with different α -MoO₃ ribbon thicknesses. The gray shaded area indicates a 5% uncertainty in the dielectric function value.

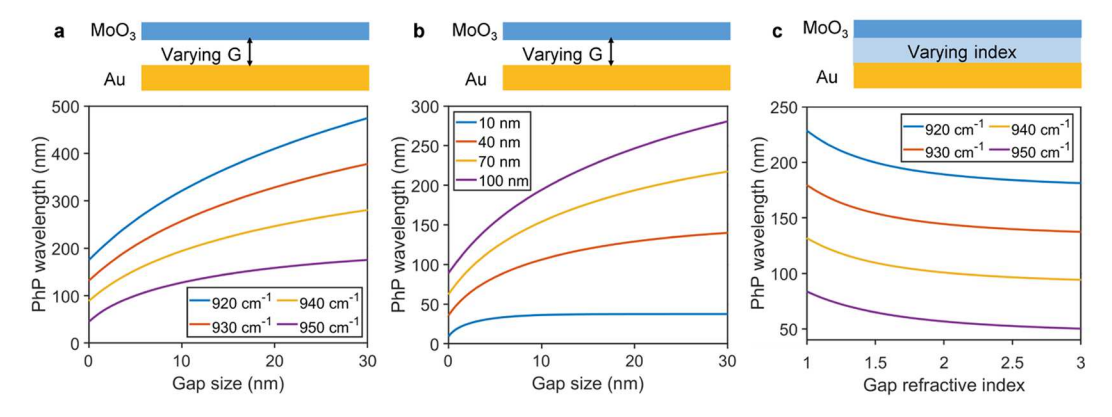


Figure 4. Theoretical PhP wavelength dependence on geometry and gap refractive index. (a) PhP wavelength versus gap size for different excitation frequencies, with the α -MoO₃ waveguide thickness fixed to 100 nm. (b) PhP wavelength versus gap size for different α -MoO₃ waveguide thicknesses, with the excitation frequency fixed to 940 cm⁻¹. (c) PhP wavelength vs gap refractive index for different excitation frequencies, with the α -MoO₃ thickness fixed to 100 nm.

displays a similar reproducible gap-dependent dispersion behavior. Figure 3d shows the gap-dependent PhP wavelength dispersion of all five tapered samples with PhP wavelengths normalized to the flake thicknesses (see the Supporting Information for further analysis). The yellow curve is the theoretical prediction from the fitted dielectric function obtained in Figure 2c and eq 1. The gray area indicates the theoretical prediction with a 5% uncertainty in the dielectric constant, within which the bulk of our data resides. We note that while the zero gap regions of these samples were used in part to evaluate α -MoO $_3$ dielectric function values, we do not expect their inclusion to bias the dielectric constant fitting process, since the extracted dielectric values from Figure 2c are from 19 total samples. We hypothesize that the observed

deviation between theoretical and experimental dispersion is from the fact that our model does not include the tilt angles of the α -MoO₃ structure or the nonadiabatic nature of the taper structure. These deviations are not due to strain effects in the tapered area, which is confirmed from Raman spectra measurements (Supporting Information).

To evaluate the sensitivity of the gap mode to various physical parameters in the taper system, we perform numerical parametric sweeps of PhP dispersion in the Reststrahlen band RB_X (along [100]) using the transfer matrix method (Figure 4 and section 7 in the Supporting Information). We observe a strong dependence of PhP wavelength on gap size, gap refractive index, ribbon thickness, and excitation frequency. These simulations indicate that while wavelength confinement

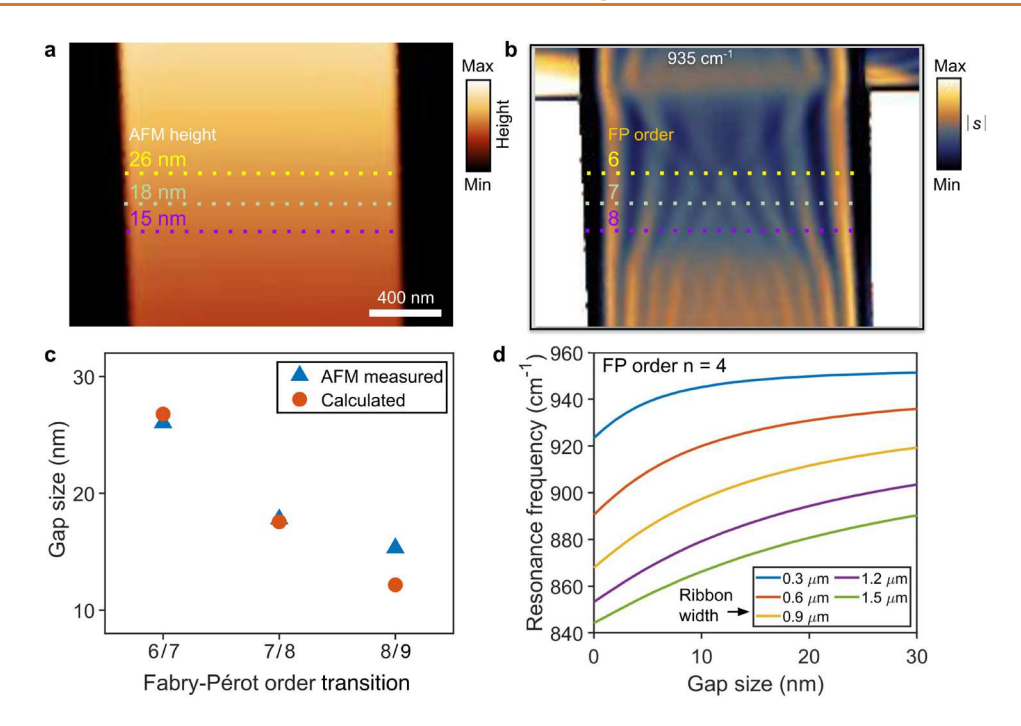


Figure 5. Resonant α -MoO₃ rulers. (a, b) Simultaneously measured AFM and SNOM images of a narrow, resonant tapered structure at 935 cm⁻¹, with dashed lines indicating the gap height and the corresponding Fabry-Pérot (FP) order transition. (c) Calculated and measured gap height for boundary regions separating Fabry-Pérot (FP) order transitions 6-8. The dielectric functions used in the calculation are specified in Figure 2c. (d) Theoretical FP resonance frequency dependence on gap size with different nanoresonator widths.

is key to the polaritonic ruler concept, extreme confinement is detrimental to ruler sensitivity: when the excitation frequency is near the longitudinal and transverse optical phonon line (963 cm $^{-1}$ LO $_1/{\rm TO}_2$) or particularly thin $\alpha\textsc{-MoO}_3$ waveguides are considered, wavelength confinement is enhanced and reduces sensitivity. This trend is due to the nature of volumetric hyperbolic modes, which can feature strong mode confinement and reduced field leakage outside the $\alpha\textsc{-MoO}_3$ layer at these limits. For the gap-filling medium refractive index dependence study (Figure 4c), the PhP wavelength is the most sensitive when the index is close to 1. This analysis is limited to relatively thick $\alpha\textsc{-MoO}_3$ layers, and for thin films close to the monolayer limit, more complex models that account for nonlocal effects $^{45-47}$ are required.

Finally, we observe that narrow tapered structures serve as hyperbolic Fabry-Pérot (FP) resonators 33,37,48 that support a simple and interpretable readout mechanism of gap dimension as a function of position upon SNOM scanning. The FP resonance order is a function of the gap dimension and transitions when reflection events destructively interfere. Interference conditions are satisfied at $2kL + 2\phi = (2n +$ $1)\pi$ for the FP order transition point, where q is the PhP mode wavevector, L is the ribbon width, 2kL is the propagation phase accumulated from a round trip across the ribbon, and ϕ is the reflection phase term. ϕ is typically $\pi/4$ for highly confined polariton modes. ⁴⁹ At nodes, the wavevector $k = ((2n + 1)\pi (2\phi)/2L$ is specified given the ribbon width. Upon integrating this model with our derived PhP mode dispersion (eq 1), we can readily correlate the positions of FP nodes with gap sizes. This spatial interferometry is unique in our system, as it features α -MoO₃ ribbons with nanoscale widths, low loss, and atomically smooth and parallel edges, all of which are required for resonant FP phenomena.

Figure 5a,b shows the correlated measured heights with the FP nodes. We first determined the position of the nodes in the SNOM image (Figure 5b), where the mode destructively interferes. We then correlate these mode transition positions with the AFM image and extract the gap sizes. Our measured AFM heights show good agreement with the calculated heights at the FP nodes in Figure 5c, which indicates that our structure can directly read out the gap sizes from the SNOM images by delineating regions of constant mode order in the images and their borders. We note that the estimated height at the region where the FP order transitions from 8 to 9 deviates from that measured in AFM, and this may be due to the noise in the SNOM image. The broad-band simulation in Figure 5d, using dielectric functions from ref 40, indicates that the FP resonances strongly depend on the excitation wavelength, 33,50,51 and this is consistent with our experimental results (see the Supporting Information for SNOM scans at 942 cm⁻¹). In this manner, the utilization of ultrabroad-band nanospectroscopy on our tapered samples can enable direct and spatially continuous readout of the gap dimension along the full taper.

CONCLUSION

In summary, we demonstrate that self-assembled taper-gapped structures serve as sensitive hyperbolic PhP-based rulers at mid-infrared wavelengths. The SNOM-based dielectric function fitting procedure that we developed provides an accurate evaluation of $\alpha\text{-MoO}_3$ ribbon dielectric functions and can be applied to other polaritonic nanomaterials, for which far-field ellipsometry cannot apply. Sufficiently narrow polaritonic rulers function as gap-dependent FP resonators, which serve as a spatial interferometer that support direct and accurate nanoruler readout.

ACS Nano www.acsnano.org Article

We anticipate various pathways for future research. Our direction is to study adiabatic polaritonic wave propagation for ultraconfined mode tuning and routing. Nanotapers have been proposed to support acoustic polaritons for extreme mode conversion in theoretical studies, 47,52 but experimental work is still absent in part because of challenges in materials preparation. Our sample structure, whose gap can be filled with vibration-active materials such as organic molecules, also is an ideal platform to tune and probe vibrational strong coupling. 16,17,53-55 While our demonstration here focuses on height or gap metrology, the structures we propose and demonstrate may also provide device concepts for passive and active spectroscopic sensing in the infrared range, such as large-area resonator arrays for far-field infrared spectroscopic sensing, which will be a scalable and efficient platform without scanning probes. 56-60

METHODS

Sample Preparation. The α -MoO₃ samples in this work were synthesized by flame vapor deposition (FVD), the details of which have been reported in our previous work.³³ Specifically, the FVD was done with a 6 cm diameter premixed flat-flame burner (McKenna burner, Holthuis & Associates) with CH₄ as the fuel and air as the oxidizer, at a fuel-to-air equivalence ratio of 0.88. A 4 cm \times 4 cm Mo mesh prepared from Mo wires (0.203 mm in diameter, 99.9%, Alfa Aesar) was placed over the premixed flame as the solid Mo source. The temperature of the solid Mo source was about 792 °C. α -MoO₃ structures were grown on a Si wafer at about 567 °C, which was placed above the Mo source. All of the α -MoO₃ samples were prepared by a 5 min deposition. The as-grown α -MoO₃ structures were then transferred onto ultrasmooth gold/glass substrates using a low-adhesion cleanroom tape (UltraTape 1310) for optical characterizations. The ultrasmooth Au substrate was template-stripped from a Si wafer (Platypus Technologies).

Near-Field Optical Imaging. PhPs in the α -MoO $_3$ nanostructures were imaged with a commercial SNOM system (Neaspec) and a tunable CO $_2$ laser (Access Laser). Sharp metal-coated tips, tapping at 280 kHz, were used to probe near-field signals in pseudoheterodyne interferometric mode. The collected light was detected with a liquid-nitrogen-cooled mercury—cadmium—telluride (MCT) detector (Kolmar KLD-0.1). The SNOM imaging was done under ambient conditions. The third-order harmonic near-field signal s_3 was presented and analyzed.

ASSOCIATED CONTENT

Supporting Information

The Supporting Information is available free of charge at https://pubs.acs.org/doi/10.1021/acsnano.3c08735.

Additional details on mode dispersion near the Reststrahlen band, derivation of analytic dispersion relations, comparison of analytic dispersion relation and TMM, phonon—polariton data fitting, dielectric function parameters and fitting, SNOM raw data of taper-gapped samples, Raman spectroscopy, derivation and experimental results of dispersion and sensitivity, measured/ calculated gap at FP nodes and antinodes, resonator effect at varied frequencies, and electric field profiles of gapped α -MoO₃ structures (PDF)

AUTHOR INFORMATION

Corresponding Author

Jonathan A. Fan – Department of Electrical Engineering, Stanford University, Stanford, California 94305, United States; orcid.org/0000-0001-9816-9979; Email: jonfan@stanford.edu

Authors

Shang-Jie Yu — Department of Electrical Engineering, Stanford University, Stanford, California 94305, United States

Helen Yao — Department of Materials Science and Engineering, Stanford University, Stanford, California 94305, United States; SLAC National Accelerator Laboratory, Menlo Park, California 94025, United States; orcid.org/0009-0004-9774-8994

Guangwei Hu − Department of Electrical Engineering, Stanford University, Stanford, California 94305, United States; orcid.org/0000-0002-3023-9632

Yue Jiang — Department of Mechanical Engineering, Stanford University, Stanford, California 94305, United States;
orcid.org/0000-0002-6017-8551

Xiaolin Zheng — Department of Mechanical Engineering, Stanford University, Stanford, California 94305, United States; orcid.org/0000-0002-8889-7873

Shanhui Fan — Department of Electrical Engineering, Stanford University, Stanford, California 94305, United States;
orcid.org/0000-0002-0081-9732

Tony F. Heinz – Department of Applied Physics, Stanford University, Stanford, California 94305, United States; SLAC National Accelerator Laboratory, Menlo Park, California 94025, United States; orcid.org/0000-0003-1365-9464

Complete contact information is available at: https://pubs.acs.org/10.1021/acsnano.3c08735

Author Contributions

#S.-J.Y. and H.Y. contributed equally to this work.

Notes

The authors declare no competing financial interest.

ACKNOWLEDGMENTS

J.A.F. acknowledges support for personnel from the Packard Fellowship Foundation and the Air Force Office of Scientific Research (AFOSR) Multidisciplinary University Research Initiative (MURI) under award no. FA9550-16-1-0031. Support for data collection was provided by Q-NEXT, supported by the U.S. Department of Energy, Office of Science, National Quantum Information Science Research Centers (H.Y.). Support for analysis and simulation was provided by the MURI on Twist Optics via the Office of Naval Research under award no.N00014-23-1-2567 and by the Gordon and Betty Moore Foundation's EPiQS Initiative through Grant GBMF9462 (T.F.H., H.Y.). Support for experimental materials growth was provided by the NSF EFRI-DCheM program under award no. SUB0000425 (X.Z.). The authors acknowledge support for experimental SNOM instrumentation from the National Science Foundation (NSF) under award no. 2103721 (J.A.F.), the AFOSR under award no. FA9550-18-1-0070 (J.A.F.), and the Department of Energy (DOE) "Photonics at Thermodynamic Limits" Energy Frontier Research Center under grant no. DE-SC0019140 (T.F.H.).

REFERENCES

(1) Sattari, H.; Graziosi, T.; Kiss, M.; Seok, T. J.; Han, S.; Wu, M. C.; Quack, N. Silicon Photonic MEMS Phase-Shifter. *Opt. Express* **2019**, 27, 18959–18969.

- (2) Errando-Herranz, C.; Colangelo, M.; Ahmed, S.; Björk, J.; Gylfason, K. B. MEMS Tunable Silicon Photonic Grating Coupler for Post-Assembly Optimization of Fiber-to-Chip Coupling. 2017 IEEE 30th International Conference on Micro Electro Mechanical Systems (MEMS), 2017; pp 293–296.
- (3) Eichenfield, M.; Chan, J.; Camacho, R. M.; Vahala, K. J.; Painter, O. Optomechanical Crystals. *Nature* **2009**, *462*, 78–82.
- (4) Leijssen, R.; La Gala, G. R.; Freisem, L.; Muhonen, J. T.; Verhagen, E. Nonlinear Cavity Optomechanics with Nanomechanical Thermal Fluctuations. *Nat. Commun.* **2017**, *8*, No. 16024.
- (5) Ma, W.; et al. In-Plane Anisotropic and Ultra-Low-Loss Polaritons in a Natural van der Waals Crystal. *Nature* **2018**, 562, 557–562.
- (6) Zheng, Z.; Xu, N.; Oscurato, S. L.; Tamagnone, M.; Sun, F.; Jiang, Y.; Ke, Y.; Chen, J.; Huang, W.; Wilson, W. L.; Ambrosio, A.; Deng, S.; Chen, H. A Mid-Infrared Biaxial Hyperbolic van der Waals Crystal. *Sci. Adv.* **2019**, *5*, 8690.
- (7) Hu, G.; Ou, Q.; Si, G.; Wu, Y.; Wu, J.; Dai, Z.; Krasnok, A.; Mazor, Y.; Zhang, Q.; Bao, Q.; Qiu, C.-W.; Alù, A. Topological Polaritons and Photonic Magic Angles in Twisted α -MoO3 Bilayers. *Nature* **2020**, *582*, 209–213.
- (8) Dai, S.; et al. Tunable Phonon Polaritons in Atomically Thin van der Waals Crystals of Boron Nitride. Science 2014, 343, 1125–1129.
- (9) Caldwell, J. D.; Kretinin, A. V.; Chen, Y.; Giannini, V.; Fogler, M. M.; Francescato, Y.; Ellis, C. T.; Tischler, J. G.; Woods, C. R.; Giles, A. J.; Hong, M.; Watanabe, K.; Taniguchi, T.; Maier, S. A.; Novoselov, K. S. Sub-Diffractional Volume-Confined Polaritons in the Natural Hyperbolic Material Hexagonal Boron Nitride. *Nat. Commun.* 2014, 5, 5221.
- (10) Li, P.; Lewin, M.; Kretinin, A. V.; Caldwell, J. D.; Novoselov, K. S.; Taniguchi, T.; Watanabe, K.; Gaussmann, F.; Taubner, T. Hyperbolic Phonon-Polaritons in Boron Nitride for Near-Field Optical Imaging and Focusing. *Nat. Commun.* **2015**, *6*, 7507.
- (11) Taboada-Gutiérrez, J.; et al. Broad Spectral Tuning of Ultra-Low-Loss Polaritons in a van der Waals Crystal by Intercalation. *Nat. Mater.* **2020**, *19*, 964–968.
- (12) Basov, D. N.; Fogler, M. M.; Abajo, F. J. G. d. Polaritons in van der Waals Materials. *Science* **2016**, *354*, No. aag1992.
- (13) Low, T.; Chaves, A.; Caldwell, J. D.; Kumar, A.; Fang, N. X.; Avouris, P.; Heinz, T. F.; Guinea, F.; Martin-Moreno, L.; Koppens, F. Polaritons in Layered Two-Dimensional Materials. *Nat. Mater.* **2017**, *16*, 182–194.
- (14) Zhang, Q.; Hu, G.; Ma, W.; Li, P.; Krasnok, A.; Hillenbrand, R.; Alù, A.; Qiu, C.-W. Interface Nano-Optics with van der Waals Polaritons. *Nature* **2021**, *597*, 187–195.
- (15) He, M.; Hoogendoorn, L.; Dixit, S.; Pan, Z.; Lu, G.; Diaz-Granados, K.; Li, D.; Caldwell, J. D. Guided Polaritons along the Forbidden Direction in MoO3 with Geometrical Confinement. *Nano Lett.* **2023**, 23, 5035–5041.
- (16) Autore, M.; Li, P.; Dolado, I.; Alfaro-Mozaz, F. J.; Esteban, R.; Atxabal, A.; Casanova, F.; Hueso, L. E.; Alonso-González, P.; Aizpurua, J.; Nikitin, A. Y.; Vélez, S.; Hillenbrand, R. Boron Nitride Nanoresonators for Phonon-Enhanced Molecular Vibrational Spectroscopy at the Strong Coupling Limit. *Light Sci. Appl.* **2018**, *7*, No. 17172.
- (17) Bylinkin, A.; Schnell, M.; Autore, M.; Calavalle, F.; Li, P.; Taboada-Gutièrrez, J.; Liu, S.; Edgar, J. H.; Casanova, F.; Hueso, L. E.; Alonso-Gonzalez, P.; Nikitin, A. Y.; Hillenbrand, R. Real-Space Observation of Vibrational Strong Coupling Between Propagating Phonon Polaritons and Organic Molecules. *Nat. Photonics* **2021**, *15*, 197–202.
- (18) Dai, S.; Tymchenko, M.; Xu, Z.-Q.; Tran, T. T.; Yang, Y.; Ma, Q.; Watanabe, K.; Taniguchi, T.; Jarillo-Herrero, P.; Aharonovich, I.; Basov, D. N.; Tao, T. H.; Alù, A. Internal Nanostructure Diagnosis with Hyperbolic Phonon Polaritons in Hexagonal Boron Nitride. *Nano Lett.* **2018**, *18*, 5205–5210.
- (19) Dai, S.; Quan, J.; Hu, G.; Qiu, C.-W.; Tao, T. H.; Li, X.; Alù, A. Hyperbolic Phonon Polaritons in Suspended Hexagonal Boron Nitride. *Nano Lett.* **2019**, *19*, 1009–1014.

- (20) Yang, J.; Tang, J.; Ghasemian, M. B.; Mayyas, M.; Yu, Q. V.; Li, L. H.; Kalantar-Zadeh, K. High-Q Phonon-polaritons in Spatially Confined Freestanding α-MoO3. *ACS Photonics* **2022**, *9*, 905.
- (21) Zheng, Z.; Sun, F.; Xu, N.; Huang, W.; Chen, X.; Ke, Y.; Zhan, R.; Chen, H.; Deng, S. Tunable Hyperbolic Phonon Polaritons in a Suspended van der Waals α -MoO3 with Gradient Gaps. *Adv. Opt. Mater* **2022**, *10*, No. 2102057.
- (22) Zhang, Q.; Ou, Q.; Hu, G.; Liu, J.; Dai, Z.; Fuhrer, M. S.; Bao, Q.; Qiu, C.-W. Hybridized Hyperbolic Surface Phonon Polaritons at α -MoO3 and Polar Dielectric Interfaces. *Nano Lett.* **2021**, 21, 3112–3119
- (23) Schwartz, J. J.; Le, S. T.; Krylyuk, S.; Richter, C. A.; Davydov, A. V.; Centrone, A. Substrate-Mediated Hyperbolic Phonon Polaritons in MoO3. *Nanophotonics* **2021**, *10*, 1517–1527.
- (24) Duan, J.; Alvarez Pérez, G.; Lanza, C.; Voronin, K.; Tresguerres-Mata, A. I. F.; Capote-Robayna, N.; Álvarez Cuervo, J.; Tarazaga Martín-Luengo, A.; Martín-Sánchez, J.; Volkov, V. S.; Nikitin, A. Y.; Alonso-González, P. Multiple and Spectrally Robust Photonic Magic Angles in Reconfigurable α -MoO3 trilayers. *Nat. Mater.* **2023**, 22, 867–872.
- (25) Sternbach, A. J.; Moore, S. L.; Rikhter, A.; Zhang, S.; Jing, R.; Shao, Y.; Kim, B. S. Y.; Xu, S.; Liu, S.; Edgar, J. H.; Rubio, A.; Dean, C.; Hone, J.; Fogler, M. M.; Basov, D. N. Negative Refraction in Hyperbolic Hetero-Bicrystals. *Science* **2023**, *379*, 555–557.
- (26) Huang, J.; Tao, L.; Dong, N.; Wang, H.; Zhou, S.; Wang, J.; He, X.; Wu, K. In-Plane Hyperbolic Phonon-Polaritons in van der Waals Nanocrystals. *Adv. Opt. Mater.* **2023**, *11*, No. 2202048.
- (27) Lee, I.-H.; He, M.; Zhang, X.; Luo, Y.; Liu, S.; Edgar, J. H.; Wang, K.; Avouris, P.; Low, T.; Caldwell, J. D.; Oh, S.-H. Image Polaritons in Boron Nitride for Extreme Polariton Confinement with Low Losses. *Nat. Commun.* **2020**, *11*, 3649.
- (28) Menabde, S. G.; Heiden, J. T.; Cox, J. D.; Mortensen, N. A.; Jang, M. S. Image Polaritons in van der Waals Crystals. *Nanophotonics* **2022**, *11*, 2433–2452.
- (29) Li, P.; Dolado, I.; Alfaro-Mozaz, F. J.; Casanova, F.; Hueso, L. E.; Liu, S.; Edgar, J. H.; Nikitin, A. Y.; Vélez, S.; Hillenbrand, R. Infrared Hyperbolic Metasurface Based on Nanostructured van der Waals Materials. *Science* **2018**, *359*, 892–896.
- (30) Sönnichsen, C.; Reinhard, B. M.; Liphardt, J.; Alivisatos, A. P. A Molecular Ruler Based on Plasmon Coupling of Single Gold and Silver Nanoparticles. *Nat. Biotechnol.* **2005**, 23, 741–745.
- (31) Reinhard, B. M.; Siu, M.; Agarwal, H.; Alivisatos, A. P.; Liphardt, J. Calibration of Dynamic Molecular Rulers Based on Plasmon Coupling between Gold Nanoparticles. *Nano Lett.* **2005**, *S*, 2246–2252.
- (32) Hill, R. T.; Mock, J. J.; Hucknall, A.; Wolter, S. D.; Jokerst, N. M.; Smith, D. R.; Chilkoti, A. Plasmon Ruler with Angstrom Length Resolution. *ACS Nano* **2012**, *6*, 9237–9246.
- (33) Yu, S.-J.; Jiang, Y.; Roberts, J. A.; Huber, M. A.; Yao, H.; Shi, X.; Bechtel, H. A.; Gilbert Corder, S. N.; Heinz, T. F.; Zheng, X.; Fan, J. A. Ultrahigh-Quality Infrared Polaritonic Resonators Based on Bottom-Up-Synthesized van der Waals Nanoribbons. *ACS Nano* **2022**, *16*, 3027–3035.
- (34) Vogel, N.; Zieleniecki, J.; Köper, I. As Flat As It Gets: Ultrasmooth Surfaces from Template-Stripping Procedures. *Nanoscale* **2012**, *4*, 3820–3832.
- (35) Naumann, R.; Schiller, S. M.; Giess, F.; Grohe, B.; Hartman, K. B.; Kärcher, I.; Köper, I.; Lübben, J.; Vasilev, K.; Knoll, W. Tethered Lipid Bilayers on Ultraflat Gold Surfaces. *Langmuir* **2003**, *19*, 5435–5443.
- (36) Olmon, R. L.; Slovick, B.; Johnson, T. W.; Shelton, D.; Oh, S.-H.; Boreman, G. D.; Raschke, M. B. Optical Dielectric Function of Gold. *Phys. Rev. B* **2012**, *86*, No. 235147.
- (37) Dai, Z.; Hu, G.; Si, G.; Ou, Q.; Zhang, Q.; Balendhran, S.; Rahman, F.; Zhang, B. Y.; Ou, J. Z.; Li, G.; Alù, A.; Qiu, C.-W.; Bao, Q. Edge-Oriented and Steerable Hyperbolic Polaritons in Anisotropic van der Waals Nanocavities. *Nat. Commun.* **2020**, *11*, 6086.
- (38) Álvarez-Pérez, G.; Voronin, K. V.; Volkov, V. S.; Alonso-González, P.; Nikitin, A. Y. Analytical Approximations for the

- Dispersion of Electromagnetic Modes in Slabs of Biaxial Crystals. *Phys. Rev. B* **2019**, *100*, No. 235408.
- (39) Menabde, S. G.; Jahng, J.; Boroviks, S.; Ahn, J.; Heiden, J. T.; Hwang, D. K.; Lee, E. S.; Mortensen, N. A.; Jang, M. S. Low-Loss Anisotropic Image Polaritons in van der Waals Crystal α -MoO3. Adv. Opt. Mater. **2022**, 10, No. 2201492.
- (40) Álvarez Pérez, G.; et al. Infrared Permittivity of the Biaxial van der Waals Semiconductor α -MoO3 from Near- and Far-Field Correlative Studies. *Adv. Mater.* **2020**, 32, No. 1908176.
- (41) Dong, W.; Qi, R.; Liu, T.; Li, Y.; Li, N.; Hua, Z.; Gao, Z.; Zhang, S.; Liu, K.; Guo, J.; Gao, P. Broad-Spectral-Range Sustainability and Controllable Excitation of Hyperbolic Phonon Polaritons in α -MoO3. *Adv. Mater.* **2020**, 32, No. 2002014.
- (42) Schoche, S.; Ho, P.-H.; Roberts, J. A.; Yu, S. J.; Fan, J. A.; Falk, A. L. Mid-IR and UV-Vis-NIR Mueller Matrix Ellipsometry Characterization of Tunable Hyperbolic Metamaterials Based on Self-Assembled Carbon Nanotubes. *J. Vac. Sci. Technol. B* **2020**, 38, No. 014015.
- (43) Dai, S.; et al. Phonon Polaritons in Monolayers of Hexagonal Boron Nitride. *Adv. Mater.* **2019**, *31*, No. 1806603.
- (44) Chen, X.; Hu, D.; Mescall, R.; You, G.; Basov, D. N.; Dai, Q.; Liu, M. Modern Scattering-Type Scanning Near-Field Optical Microscopy for Advanced Material Research. *Adv. Mater.* **2019**, *31*, No. 1804774.
- (45) Lundeberg, M. B.; Gao, Y.; Asgari, R.; Tan, C.; Van Duppen, B.; Autore, M.; Alonso-González, P.; Woessner, A.; Watanabe, K.; Taniguchi, T.; Hillenbrand, R.; Hone, J.; Polini, M.; Koppens, F. H. L. Tuning Quantum Nonlocal Effects in Graphene Plasmonics. *Science* 2017, 357, 187–191.
- (46) Gubbin, C. R.; De Liberato, S. Optical Nonlocality in Polar Dielectrics. *Phys. Rev. X* **2020**, *10*, No. 021027.
- (47) Yuan, Z.; Chen, R.; Li, P.; Nikitin, A. Y.; Hillenbrand, R.; Zhang, X. Extremely Confined Acoustic Phonon Polaritons in Monolayer-hBN/Metal Heterostructures for Strong Light–Matter Interactions. ACS Photonics 2020, 7, 2610–2617.
- (48) Roberts, J. A.; Yu, S.-J.; Ho, P.-H.; Schoeche, S.; Falk, A. L.; Fan, J. A. Tunable Hyperbolic Metamaterials Based on Self-Assembled Carbon Nanotubes. *Nano Lett.* **2019**, *19*, 3131–3137.
- (49) Kang, J.-H.; Wang, S.; Shi, Z.; Zhao, W.; Yablonovitch, E.; Wang, F. Goos-Hänchen Shift and Even—Odd Peak Oscillations in Edge-Reflections of Surface Polaritons in Atomically Thin Crystals. *Nano Lett.* **2017**, *17*, 1768—1774.
- (50) Roberts, J. A.; Ho, P.-H.; Yu, S.-J.; Wu, X.; Luo, Y.; Wilson, W. L.; Falk, A. L.; Fan, J. A. Multiple Tunable Hyperbolic Resonances in Broadband Infrared Carbon-Nanotube Metamaterials. *Phys. Rev. Appl.* **2020**. *14*. No. 044006.
- (51) Deng, G.; Dereshgi, S. A.; Song, X.; Wei, C.; Aydin, K. Phonon-Polariton Assisted Broadband Resonant Absorption in Anisotropic α -phase MoO3 Nanostructures. *Phys. Rev. B* **2020**, *102*, No. 035408.
- (52) Voronin, K. V.; Aseguinolaza Aguirreche, U.; Hillenbrand, R.; Volkov, V. S.; Alonso-González, P.; Nikitin, A. Y. Nanofocusing of Acoustic Graphene Plasmon Polaritons for Enhancing Mid-Infrared Molecular Fingerprints. *Nanophotonics* **2020**, *9*, 2089–2095.
- (53) Epstein, I.; Alcaraz, D.; Huang, Z.; Pusapati, V.-V.; Hugonin, J.-P.; Kumar, A.; Deputy, X. M.; Khodkov, T.; Rappoport, T. G.; Hong, J.-Y.; Peres, N. M. R.; Kong, J.; Smith, D. R.; Koppens, F. H. L. Far-Field Excitation of Single Graphene Plasmon Cavities with Ultra-compressed Mode Volumes. *Science* **2020**, *368*, 1219–1223.
- (54) Garcia-Vidal, F. J.; Ciuti, C.; Ebbesen, T. W. Manipulating Matter by Strong Coupling to Vacuum Fields. *Science* **2021**, *373*, No. eabd0336.
- (55) Liu, K.; Huang, G.; Li, X.; Zhu, G.; Du, W.; Wang, T. Vibrational Strong Coupling between Surface Phonon Polaritons and Organic Molecules via Single Quartz Micropillars. *Adv. Mater.* **2022**, 34, No. 2109088.
- (56) Hu, H.; Yang, X.; Guo, X.; Khaliji, K.; Biswas, S. R.; García de Abajo, F. J.; Low, T.; Sun, Z.; Dai, Q. Gas Identification with Graphene Plasmons. *Nat. Commun.* **2019**, *10*, 1131.

- (57) Roberts, J. A.; Ho, P.-H.; Yu, S.-J.; Fan, J. A. Electrically Driven Hyperbolic Nanophotonic Resonators as High Speed, Spectrally Selective Thermal Radiators. *Nano Lett.* **2022**, *22*, 5832–5840.
- (58) Bareza, N. J.; Paulillo, B.; Slipchenko, T. M.; Autore, M.; Dolado, I.; Liu, S.; Edgar, J. H.; Vélez, S.; Martín-Moreno, L.; Hillenbrand, R.; Pruneri, V. Phonon-Enhanced Mid-Infrared CO2 Gas Sensing Using Boron Nitride Nanoresonators. *ACS Photonics* **2022**, *9*, 34–42.
- (59) Baumberg, J. J.; Aizpurua, J.; Mikkelsen, M. H.; Smith, D. R. Extreme Nanophotonics from Ultrathin Metallic Gaps. *Nat. Mater.* **2019**, *18*, 668–678.
- (60) Altug, H.; Oh, S.-H.; Maier, S. A.; Homola, J. Advances and Applications of Nanophotonic Biosensors. *Nat. Nanotechnol.* **2022**, *17*, 5–16.